Chemically Engineered Graphene-Based 2D Organic Molecular Magnet

Jeongmin Hong,[†,*] Elena Bekyarova,[‡] Walt A. de Heer,[||] Robert C. Haddon,[‡] and Sakhrat Khizroev[§,⊥]

[†]Electrical Engineering and Computer Sciences, University of California, Berkeley, California 94720, United States, [‡]Department of Chemistry and Center for Nanoscale Science and Engineering, and [§]Department of Electrical Engineering, University of California, Riverside, California 92521, United States, [||]School of Physics, Georgia Institute of Technology, Atlanta, Georgia 30332, United States, and [⊥]Center for Personalized Nanomedicine, Florida International University, Miami, Florida 33174, United States.

ABSTRACT
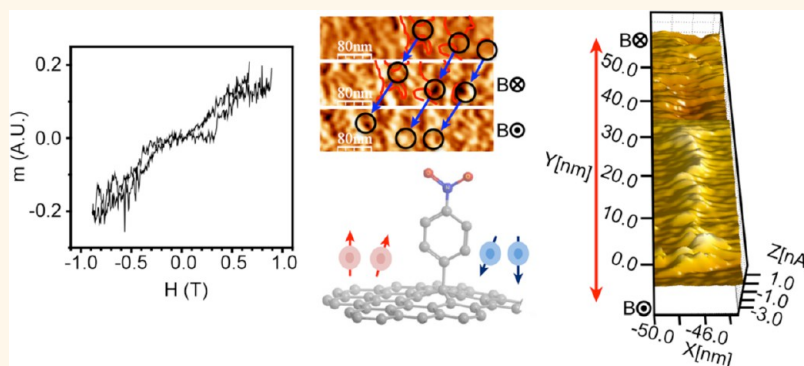
Carbon-based magnetic materials and structures of mesoscopic dimensions may offer unique opportunities for future nanomagnetoelectronic/spintronic devices. To achieve their potential, carbon nanosystems must have controllable magnetic properties. We demonstrate that nitrophenyl functionalized graphene can act as a room-temperature 2D magnet. We report a comprehensive study of low-temperature magnetotransport, vibrating sample magnetometry (VSM), and superconducting quantum interference (SQUID) measurements before and after radical functionalization. Following nitrophenyl (NP) functionalization, epitaxially grown graphene systems can become organic molecular magnets with ferromagnetic and antiferromagnetic ordering that persists at temperatures above 400 K. The field-dependent, surface magnetoelectric properties were studied using scanning probe microscopy (SPM) techniques. The results indicate that the NP-functionalization orientation and degree of coverage directly affect the magnetic properties of the graphene surface. In addition, graphene-based organic magnetic nanostructures were found to demonstrate a pronounced magneto-optical Kerr effect (MOKE). The results were consistent across different characterization techniques and indicate room-temperature magnetic ordering along preferred graphene orientations in the NP-functionalized samples. Chemically isolated graphene nanoribbons (CINs) were observed along the preferred functionality directions. These results pave the way for future magnetoelectronic/spintronic applications based on promising concepts such as current-induced magnetization switching, magnetoelectricity, half-metallicity, and quantum tunneling of magnetization.

KEYWORDS: graphene · epitaxial graphene · nitrophenyl functionalized graphene · magnetism · magnetic graphene · chemically isolated nanoribbons (CINs)

The past several years have been a golden age for carbon-based materials and structures.[1–7] Given the inherent benefits of the covalent C—C bonds in applications involving carbon-based nanomaterials, extensive efforts have been made toward controlling the electronic and magnetic properties of sp[2]-bonded carbon materials and understanding the chemical conditions that lead to stable, magnetically ordered states. The interest in carbon-based

magnetic nanostructures has also been driven by their great potential to positively impact the emergence of spintronic applications based on magnetic semiconductors.[8–13]

Graphite systems display paramagnetism due to disordered spins at irregular surfaces and the high density of step edges in bulk materials.[14,15] Ferromagnetic and superconducting orderings have also been observed in samples processed under various experimental conditions.[16,17] The ferromagnetism

in these systems is usually attributed to physical defects.[9,15,18−20] For instance, in a recent study of highly oriented pyrolytic graphite (HOPG), the origin of the ferromagnetism was ascribed to localized electronic states at the grain boundaries forming two-dimensional (2D) arrays of point defects; nevertheless, this question remains open.[21,22]

Graphene provides a perfect platform for observing the spectacular physical properties of 2D carbon systems without the complications that arise from electron interactions through a third dimension, as occurs in HOPG. However, the effects from the edges and the isolated ribbons become significant when measuring the characteristics of the basal plane. Superparamagnetic ordering has previously been observed in second- and third-stage graphite intercalation compounds.[22] Relatively strong paramagnetic ring currents have been reported in alkali metal-intercalated graphite.[23] For example, paramagnetism has been observed in graphene samples exfoliated from graphite crystals with a high density of edges and defects,[24−26] and ferromagnetic ordering has been observed in reduced graphene oxide systems.[27−29] The first report on the ferromagnetism of pure graphene systems indicated that epitaxially grown graphene with radical functionalization could exhibit mixed states of superparamagnetic, anti(ferro-)magnetic, ferrimagnetic, and ferromagnetic behaviors from low temperature to room temperature and above, depending on the functional coverage of the carbon atoms.[12] Reproducible results on the hydrogenation[30,31] of epitaxial graphene and tetracyano-p-quinodimethane molecules deposited onto epitaxial graphene on Ru (0001) were subsequently reported to give rise to ferromagnetism.[32] Separate studies have demonstrated the spin-half paramagnetism and the dual origin of magnetism in exfoliated graphene.[33] However, most reports rely on volume- and surface-averaged magnetometry, such as SQUID and magnetic force microscopy (MFM), performed on the macroscale. Thus far, no reports that provide comprehensive evidence for either macro- or nanoscale magnetic phenomena for the ferromagnetism of carbon nanostructures in chemically functionalized graphene structures have appeared in the literature.

The controlled growth of epitaxial graphene on SiC crystals makes possible the application of covalent chemistry for modifying the electron structure of the chemically pure, crystalline graphene state.[1,2,4] In addition to the current emphasis on optimizing the crystalline order, interest in understanding the chemical reactivity and its control has been rapidly growing. Optimizing the covalent chemistry of graphene requires the development of analytical techniques to quantify the formation of C−C bonds[34−36] and systematic methods for relating changes in the electronic and magnetic properties to chemical reactions and the

graphene characteristics.[37−40] We previously reported the results of macroscale volume-average and surface-average magnetometry.[12,36] Scanning tunneling microscopy (STM) was performed while observing the local density of states (LDOS) in the presence of an external magnetic field.[41] The measurements clearly indicated the existence of magnetoelectric effects in NP-functionalized graphene samples. The results of the surface measurements were in agreement with the results of the volume studies and, in addition, showed ferromagnetically and antiferromagnetically ordered states along the graphene orientations with attached functionalities. Nevertheless, because of the low sample volume and surface area of the functionalized magnetic regions, it was difficult to perform sufficiently robust measurements. Although the results indicated that the unpaired spins originated from the functionalized carbon sites, the underlying physics of the magnetic state of graphene in both its pristine and NP-functionalized forms remains to be adequately addressed.

The detection of the response from a pure magnetic phase on an atomically 2D structure under ambient conditions is challenging because the generated magnetic signal (from a few electrons) is extremely weak, even in the high-density magnetic configuration. The significant surface inhomogeneity of the graphene surface prevents long-range ferromagnetic alignment between neighboring unpaired spins. As a result, only a relatively small fraction of the sample can generate a net nonzero magnetic signal. Further, the relatively small effective size of the regions often results in superparamagnetism, which renders identification of the magnetic order type (ferro-, antiferro-, or ferrimagnetic) at room temperature even more difficult. The current study was performed on epitaxial graphene systems prepared through a covalent chemical reaction.[34−36] One of the important goals was to understand how the observed magnetic and magnetotransport properties are related to the physical properties of the graphene sample. The results obtained using a high-resolution field-dependent integrated SPM approach, which includes MFM, electric force microscopy (EFM), and STM modules, are emphasized to understand the spin configurations in 2D systems of pristine and functionalized graphene. We correlate the results of an SPM-based surface study with the results of anisotropic volume VSM and SQUID magnetometry and cryogenic magnetoresistance measurements. To the best of our knowledge, this work represents the first demonstration of directional f-MOKE surface studies of graphene and the correlation of the results with those from other studies. The observed spin alignment was correlated with the preferred graphene orientations. The current methodology can potentially enable control of the spin configurations and thus advance the covalent chemistry of graphene for emerging nanomagnetic/spintronic applications.

RESULTS AND DISCUSSION

Applied-Field Scanning Probe Microscopy. The magnetic response of pristine and functionalized graphene films was studied using applied-field magnetic force microscopy (AF-MFM) at room temperature. Figure 1 presents high-resolution atomic force micrographs of an epitaxially grown graphene sample (A) before and (B) after NP-functionalization. This high-resolution technique enables detection of the atomic structure of 2D carbon systems under ambient conditions. These measurements ensure that the starting materials are crystalline and contain no defects or impurities. The functionalities with a characteristic size of a few nanometers were formed on the basal plane of the graphene structure.

The relatively small coercive field of the functionalized graphene layer (~100 Oe), compared to the characteristic field of the MFM probe, which is on the order of a few hundred oersteds, makes it difficult to separate the magnetic information from the topography of the surface. Another challenge is the separation of the magnetic and electric interactions between the probe and the sample surface; this problem is due to the relatively low conductivity of the graphene sample and the resulting electrostatic charge that, in turn, induces a stray electric force between the sample and the probe. As described below, the (apparently) pristine areas also exhibit nonzero magnetic moments; however, in this case, separating the relatively weak magnetic signal from the electrostatic charge effects remains difficult due to the low conductivity of the sample.[12,42] To differentiate between the described side effects (topography and electric field), in addition to MFM, field-dependent EFM and STM were performed on the same samples. Further, we have used multiple probe types, with different conductivities and magnetic properties, to image the same surface. To distinguish the EFM signal, we used a gold-coated tip under a magnetic field, for which we measured the layer-dependent electrostatic charge effects.[42] As described below, after the functionalization procedure, the magnetic signal greatly overshadowed the other field effects.

Figure 1C,D shows AFM and MFM images of a pristine region with a distinct 50 nm high ripple. For the purpose of equivalent comparison, we maintained the same conditions during all of the experiments. The clear distinction between the AFM (Figure 1C) and MFM (Figure 1D) images indicates the negligible contribution of the sample topography to the magnetic signal. However, when we conducted the same measurements on the functionalized sample, the MFM image (Figure 1E) could not be fully separated from the AFM image (Figure 1F). To eliminate the surface morphology effects from the magnetic image, MFM was conducted in the presence of a variable magnetic field, as described below.
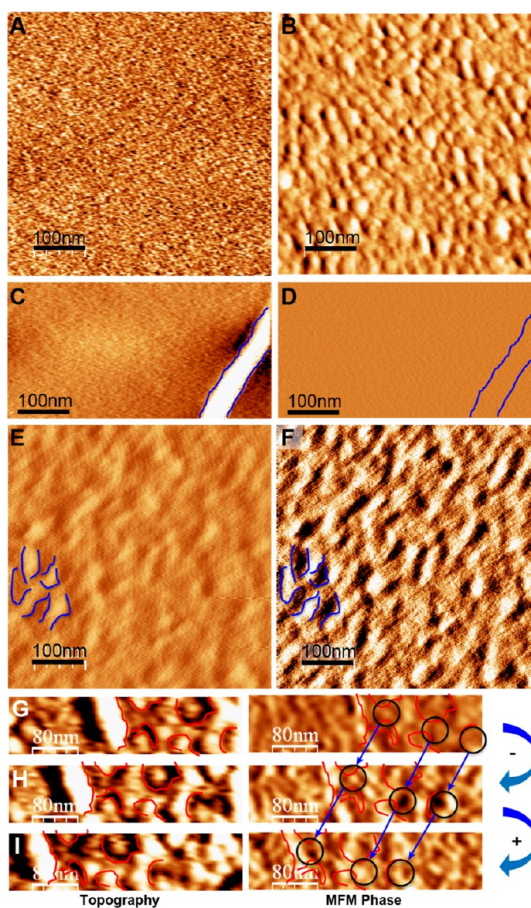

Figure 1. Ultrahigh-resolution topographical images of pristine (A) and functionalized (B) epitaxial graphene. (C) AFM image of pristine graphene and a 50 nm high ripple. (D) MFM image of pristine graphene. Note that MFM did not detect topographical effects on the 50 nm high ripple. (E) AFM image of functionalized graphene. Note the ultrahigh-resolution AFM with an interleave mode of functionalized graphene. (F) MFM image of functionalized graphene. Magnetic phase dynamics as a function of the magnetic field (G) at 0 Oe, (H) −60 Oe, and (I) +60 Oe of the functionalized graphene.

Given the small coercive field of the graphene surface and the contribution of the magnetic tip, the in-plane magnetic configuration must depend on the distance between the tip and the surface (as we observed). One of the most critical problems with the use of MFM in imaging graphene is its relatively low spatial resolution (~>10 nm). For comparison, the characteristic separation between adjacent carbon atoms in graphene is below 0.15 nm.

Furthermore, even low-moment probes can generate a local field of higher than 100 Oe, which would overwhelm any periodic magnetic superlattice that has characteristic exchange and anisotropy fields smaller than this value. Therefore, it was not surprising that the graphene samples under study acted as a soft magnetic material relative to the field generated by the CoCr-based MFM probe (approximately 0.5 kOe). Variable-field-environmental scanning probe microscopy provides a good alternative to exclude the topological

and electrical effects from the MFM measurements *via* signal differentiation approaches. This technique allows for an investigation of the local effects and field-dependent dynamics of the phase induced by the magnetic ordering, which, in turn, helps improve the magnetic image quality. For example, the field-dependent dynamics of the magnetic configuration on the functionalized graphene surface are shown in Figure 1G, H, and I. It can be seen that a 100 Oe field indeed can change the magnetic state of the sample. Ideally, the phase shift $\Delta\varphi$, as measured *via* dynamic mode MFM, should be proportional to the magnetic field gradient $\partial F/\partial z$, which depends on $z^{-5} = (h + \delta)^{-5}$, where h is the preset scanning distance between the tip's apex and the sample surface and δ is the distance between the apex and the effective position of the magnetic moment in the tip. During MFM measurement (magnetic phase response $\Delta\varphi(h)$), we could estimate that $\delta \sim$ 100 nm. Given this value, the estimated maximum magnetic moment observed by the tip is $m_{eff} \sim 6 \times 10^{-15}$ Am^2 for the area with the largest magnetic moment. The δ depends on the magnetic properties of the measured surface onto the functionalized sites. Therefore, the magnetic moment m_2 at the presence of m_1 extracted from the MFM data should only be considered as a rough estimate in dynamic mode MFM technique. Assuming that the magnetic moment measured by MFM corresponds to a region with a surface area of ~ 5 nm^2 and a depth of ~ 10 nm (as estimated by AFM topographs), we can roughly estimate the total saturation magnetic moment, as measured *via* conventional magnetometry, to be $m_s \approx [6 \times 10^{-15} \times 4\pi \times (5 \times 10^{-7})^2/(5 \times 10^{-18})] \times 10^3$ emu $\approx 4 \times 10^{-6}$ emu, which is in agreement with the results of the m-H loops measurement. If a 60 Oe field were swept, a flip in the magnetic phase would indicate the presence of antiferromagnetically coupled regions in the out-of-plane component. The overall MFM signal demonstrates the inhomogeneous distribution of the magnetically divided domains in the nitrophenyl-functionalized epitaxial graphene.

Magneto-Optical Kerr Effects. Volume- and surface-averaging methods such as VSM and SQUID lack a controllable metrology of the transition from a non-ferromagnetic material to a ferromagnetic functionalized nanocarbon structure. When the sample is transferred into a deep Dewar flask, it can become contaminated through contact with the interior wall of the Dewar. X-ray magnetic circular dichroism (XMCD) microscopy, including soft X-ray techniques using a synchrotron, could provide strong evidence of ferromagnetism in carbon structures on the nanometer scale; however, carbon contamination during the measurement is a serious limiting factor. Noninvasive localized optical measurements could provide an alternative by significantly reducing the likelihood of unwanted Fe-based impurities and other deteriorating factors. A locally focused light source can track the regional characteristics of 2D systems, especially by controlling the magnetic properties of the chemical functionality.

Recent progress in the Faraday effect of pristine graphene structures has indicated a large rotation due to the resonances that originate from the cyclotron effect and inter-Landau level (LL) transitions.[43] Moreover, a recent *ab initio* calculation indicated the presence of nonzero off-diagonal components and thus predicted Kerr and Faraday effects in functionalized graphene systems.[44] The Faraday effect is the rotation of light polarization that arises as light passes through a medium in a magnetic field; this phenomenon is the optical analogue of the Hall effect and combines a sensitivity to the carrier type with access to a broad range of energies. The purpose of magneto-optical Kerr effect (MOKE) microscopy is to detect changes in the intensity of light reflected from magnetized media. Both the polarization and reflectivity of a laser beam can be altered by the magnetized surface. Both effects result from the nonzero off-diagonal components of the dielectric tensor.

We performed MOKE microscopy to confirm the results of our other magnetometry measurements (VSM and SQUID). Local noninvasive magnetometry is important for confirming magnetic properties because a change in the local region offers an extreme mechanism to prevent possible impurities and demonstrates the systematic characteristics of the sample in different functionalized regions. Due to the relatively large material transparency, to demonstrate the out-of-plane characteristics at room temperature, we measured the polar Kerr effect in the transmission mode (Faraday effect) with a focused light source ($\sim 1\ \mu m$ in diameter). Experimental schematics are shown in Figure 2.

The data for the pristine sample were subtracted from the data for the functionalized graphene, and a linear relationship was observed at room temperature. The subtraction process is described in detail in Figure S3. After subtraction of the pristine loops from the functionalized signals, the final products of the m-H loops from the MOKE were obtained. The measured magnetic moment was removed *via* subtraction to yield the characteristics of the chemical functionalization of graphene. From these measurements, we observed antiferromagnetic alignment in perpendicular directions. Figure 2C shows the magnetic moment of the functionalized samples as a function of the magnetic field with the different locations. A diamagnetic background is characteristic of epitaxial graphene and has been observed in other carbon materials.[14] The subtracted result reflects the properties of the chemically functionalized graphene and demonstrates a clear hysteresis with a coercive field, H_c, on the order of 100 Oe, as shown in Figure 2. These results are in agreement with the results of previous VSM and SQUID measurements.
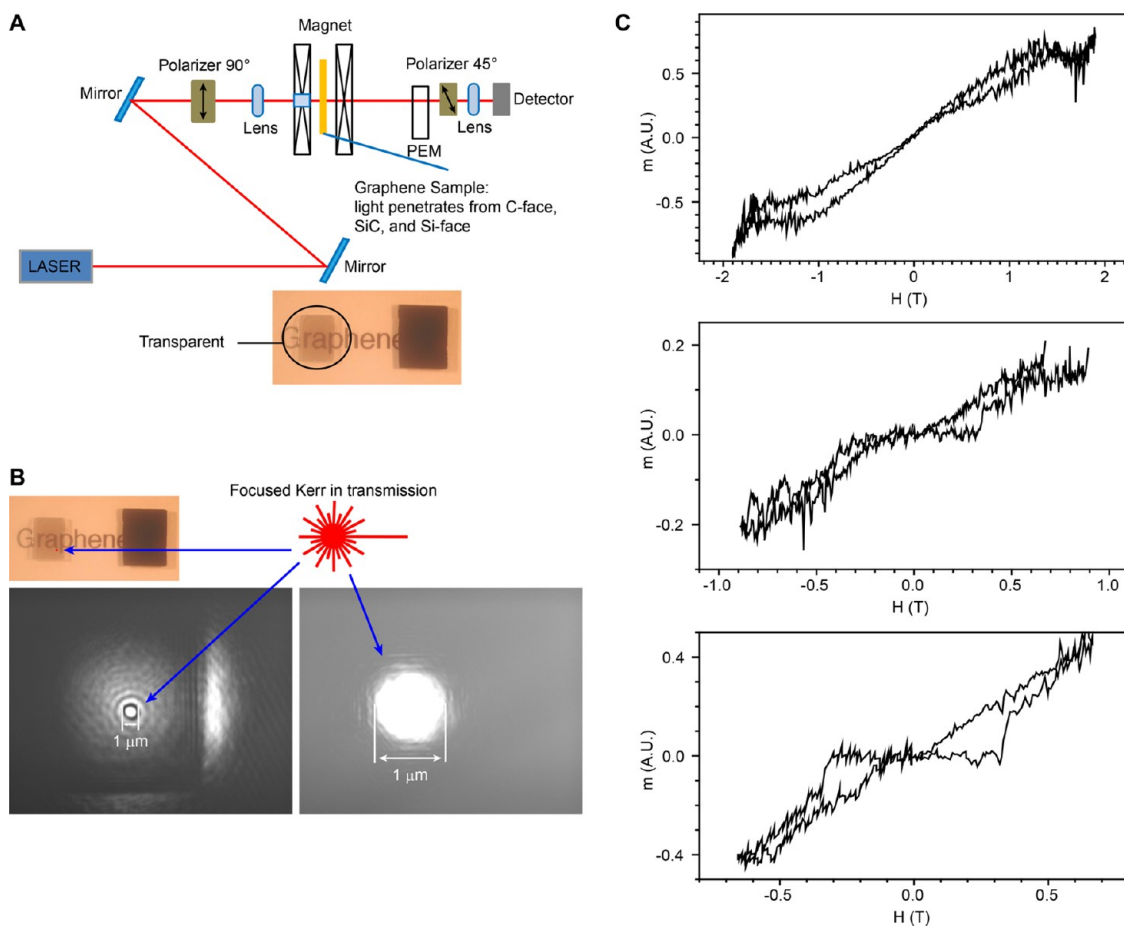
Figure 2. (A) Schematic of the focused polar magneto-optical Kerr effects in the transmission (Faraday effects) experimental setup. (B) Micrographs of a focused light source and a picture of the graphene sample (left) with a silicon chip (right) for comparison. (C) Three typical results of the m-H loops of different regions for the out-of-plane component.

Table S1 shows the exchange bias field for different regions of the functionalized graphene sample. The spin exchange bias is an indication of an antiferromagnetic coupling in the out-of-plane component; this bias field indicates that the magnetic moment of the magnetically hard portion of the antiferromagnetically coupled region causes a shift in the magnetization curve of its magnetically soft counterpart. The spin exchange bias field provides the ability to fix the magnetization direction through dipole coupling. This property could account for the GMR-like effect of negative magnetoresistance observed for the functionalized graphene at lower temperatures, as described in the next section. In summary, the described functionalized graphene nanostructures exhibited Kerr and Faraday effects, which in turn reflected a long-range magnetic order in these samples.

Volume- and Surface-Averaged Magnetometry. We performed cryogenic magnetometry measurements of the functionalized graphene using VSM and SQUID. Figure 1 shows AFM micrographs of epitaxially grown graphene before and after functionalization at ultrahigh resolution. To trigger the magnetic characteristics in the macro-level epitaxial graphene samples, we

measured m-H loops using SQUID and VSM measurements. Again, the characterization of magnetic properties in a single graphene layer of these samples is a significant challenge when using conventional methods for magnetization measurements, such as SQUID and VSM, and the diamagnetism of graphene is not expected to be observable in the presence of the SiC wafers. To obtain a pure signal arising from the functionalization, we measured and subtracted the diamagnetism of the pristine epitaxial graphene samples on the SiC, -13×10^{-5} emu/mol; to investigate the change in magnetic properties of the epitaxial graphene resulting from the chemical reaction, we subtracted measurements of the pristine sample from identical measurements obtained after the reaction.[12]

As shown in Figure 3, the m-H loops from the VSM and SQUID measurements indicate the presence of both ferromagnetic and antiferromagnetic regions in the samples. The in-plane measurements show hysteresis loops, which are characteristic of either a ferromagnetic or an antiferromagnetic material with some remnant magnetization and an easy axis normal to the plane. However, the out-of-plane measurements display a smaller remnance, instead showing the double
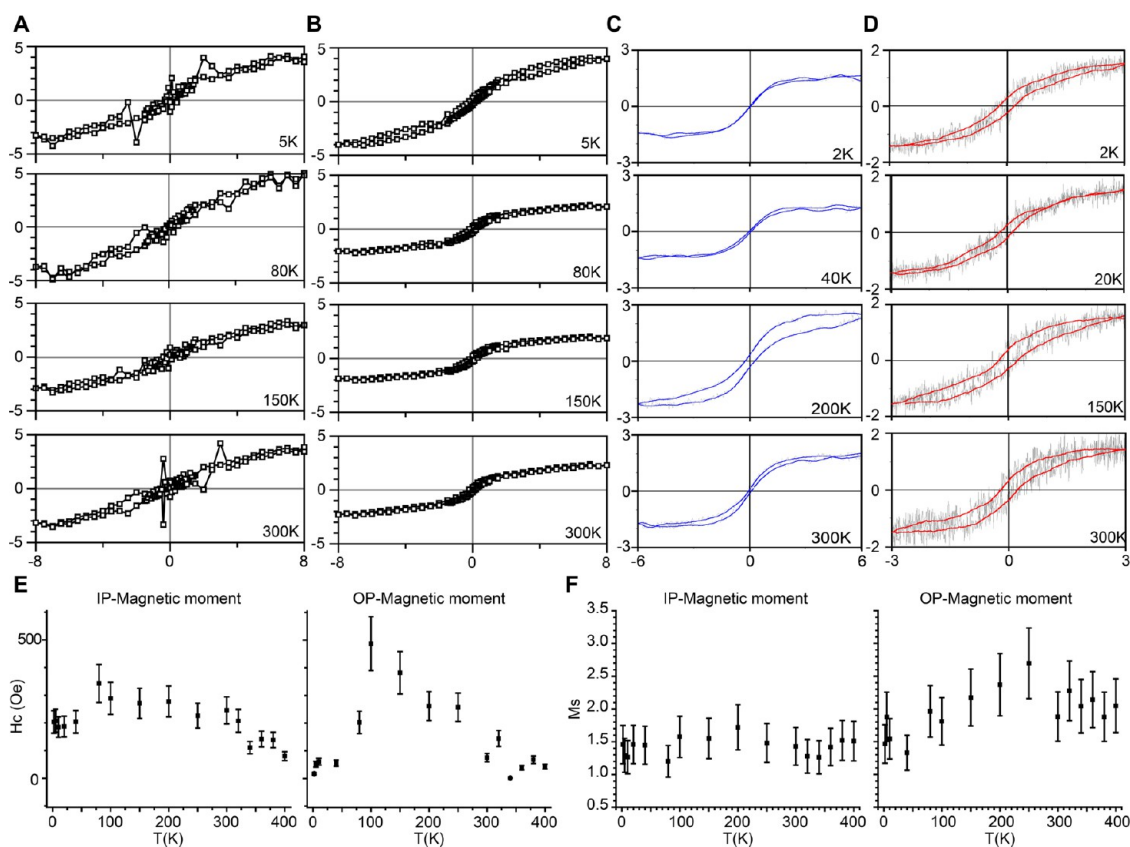
Figure 3. m-H loops of the out-of-plane component (A) over four different temperature ranges. (B) In-plane case acquired through SQUID measurements. (C) m-H loops of the out-of-plane component obtained from VSM measurements. (D) VSM measurement of the in-plane component. Temperature dependence of the coercivity (E) and magnetization (F) in the out-of-plane and in-plane directions.

loops that are typical of antiferromagnetically coupled materials with the easy axis normal to the plane. This result is in agreement with the out-of-plane data from the MOKE analysis.

We provide a schematic illustration for the mechanism of the spin switching in the hysteresis loops that is observed in the antiferromagnetic case. Note that the anisotropy field required to rotate the magnetization by 90° is on the order of 1 kOe at room temperature. The similarity in the shapes of the two curves indicates the presence of a relatively small out-of-plane anisotropy field. Figure S4 provides a schematic diagram that explains one possible route for the spin switching in the hysteresis loops in the antiferromagnetic case. The relatively "noisy" opening in the in-plane case is likely due to the hysteresis in the exchange coupling process when the spins are rotated with respect to each other as the field is applied normal to their axis. Similarly, the two symmetric openings in the out-of-plane case can be explained by the hysteresis in the exchange coupling dynamics because the field along the axis flips one of the two spins. Based on this model, the characteristic field in the two cases is defined by the exchange-coupling field ($\sim$100 Oe).

Both the in-plane and out-of-plane measurements showed a relatively low value for the saturation

magnetization of the pristine samples at room temperature (less than 2 emu/cc). Functionalization increased this value by a factor of approximately 50 at room temperature. The m-H loops for the in-plane and out-of-plane measurements of the functionalized sample are shown in Figure S2A and B, respectively. The room-temperature value for the saturation magnetization of approximately 100 emu/cc corresponds to approximately 0.1 μ_B (Bohr magnetons) per carbon atom for the NP-EG samples. Considering that there are approximately five carbon atoms per nitrophenyl group, we estimated that each functionalized site contributed approximately 0.5 μ_B (the saturation magnetization of iron is $\sim$2.2 μ_B per atom), as we reported previously.[12]

Magnetometry of Chirality. One of the most significant aspects of this research is the anisotropy examination of complete 2D structures. Magnetization intrinsically prefers to lie along an easy axis. Anisotropy is displayed in a number of properties. For example, anisotropy helps reduce the magnitude of thermal fluctuations and can modify the current flow. It also can induce relatively new phenomena, such as quantum tunneling of magnetization and the ultralow spin switching with relatively long spin relaxation time.[45,46] Systematic measurements of graphene samples with large
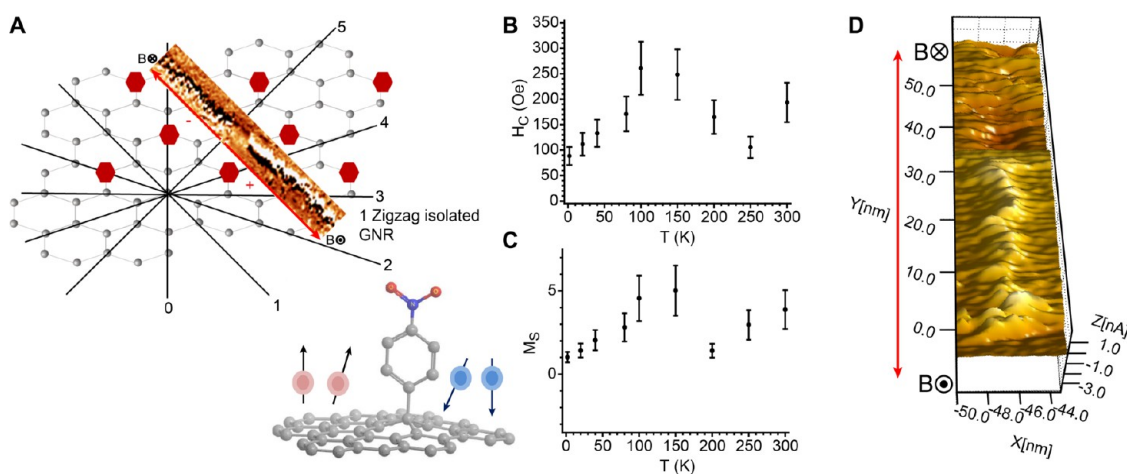
Figure 4. (A) Possible scenario for the presence of chemically isolated graphene nanoribbons (CINs). Rotation of the m-H loops (in-plane rotation by 30°) and temperature-dependent coercive field (B) and saturation magnetization (C) as a function of temperature. (D) Field-applied STM image from +100 Oe to −100 Oe along the *y*-direction.

areas can provide plane-dependent magnetization. If sufficiently strong, magnetic anisotropy can prevent rotation of the magnetization from the in-plane to the perpendicular direction due to the 2D features that arise from functionalized epitaxial graphene.

To observe the effects of chirality, we performed in-plane measurements with a rotation from 0 to 180° (in increments of 30°) using a vibrating sample magnetometer. As shown in the SI, the addition of products **3** and **4** is preferred: product **4** itself is expected to be ferromagnetic. Product **3** (formally spin-paired (antiferromagnetic) Kekule products) is expected to be diamagnetic, but is considered to be antiferromagnetc, and products **3** and **4** form graphene nanoribbons along an axis.[36] If product **3** is considered to have antiferromagnetic ordering, we could expect both antiferromagnetic behavior and ferromagnetic nanoribbons. These results support the idea that the intensity of the magnetic moment differs for different functionality orientations. The magnetization amplification for temperatures up to 400 K indicates the presence of chirality, which results from isolated carbon atoms surrounded by functionalities, as shown in Figure 4A−C. The subtraction data at 0° display the directional effects of the functionality on the basal plane of the graphene. The results indicate that the favorable addition of a functionality results in the presence of isolated nanoribbon-like carbon structures surrounded by a radical functionality. In our previous communication, we reported 2D nanoribbon structures, which indicate that 2D nanoribbons result from isolated carbon structures surrounded by radical functionalization. The Curie temperature predicted for the structure is much higher than room temperature, as shown in Figure 4C. The arrangement of the functionality can result in isolated nanoribbons, and these 1D nanoribbons play a significant role in amplifying the magnetic moment throughout the entire temperature

range. This effect makes a significant contribution to the ferromagnetic behavior from the in-plane component. One possible scenario is that the symmetry is broken by the functionalized sites, which could result in an amplification of the ferromagnetism in a specific direction. The applied field STM measurements show clear magnetization along the 1D CINs, as shown in Figure 4D.

As shown in Figure 4A, the isolated nanoribbons surrounded by the radical functionality formed in specific directions. These isolated nanoribbons amplify the magnetization by a factor of 10. Due to their potential half-metallicity, energy gap, and ferromagnetism, 1D zigzag nanoribbons have recently attracted much attention. In contrast, the isolated, functionalized graphene nanoribbons could behave as 1D chemically isolated zigzag nanoribbons. The rotation measurements indicate that the aryl radical functionality acts as an isolated ferromagnet.[10,11] As shown in Figure 4A, the possible functionality on the carbon atoms may represent the formation of isolated nanoribbons in specific directions, and this formation could result in flipping caused by the field applied during STM. Similar results have been recently reported by different groups.[31] With a favored direction, this phenomenon might only occur in isolated graphene with H-, N-, or O-atoms onto the basal plane of the graphene structure. The results indicate that chemically isolated nanoribbons (CINs) are present in preferred graphene directions, as shown in Figure 4A. In the pristine graphene case, we did not observe this amplification. Therefore, the origin of the ordered states along the preferred graphene orientations is affected by the functionalization along these orientations.

Cryogenic Magnetotransport Measurements. Cryogenic magnetotransport measurements were conducted, in which the electrons in the graphene undergo a quantum mechanical interference. This interference renders
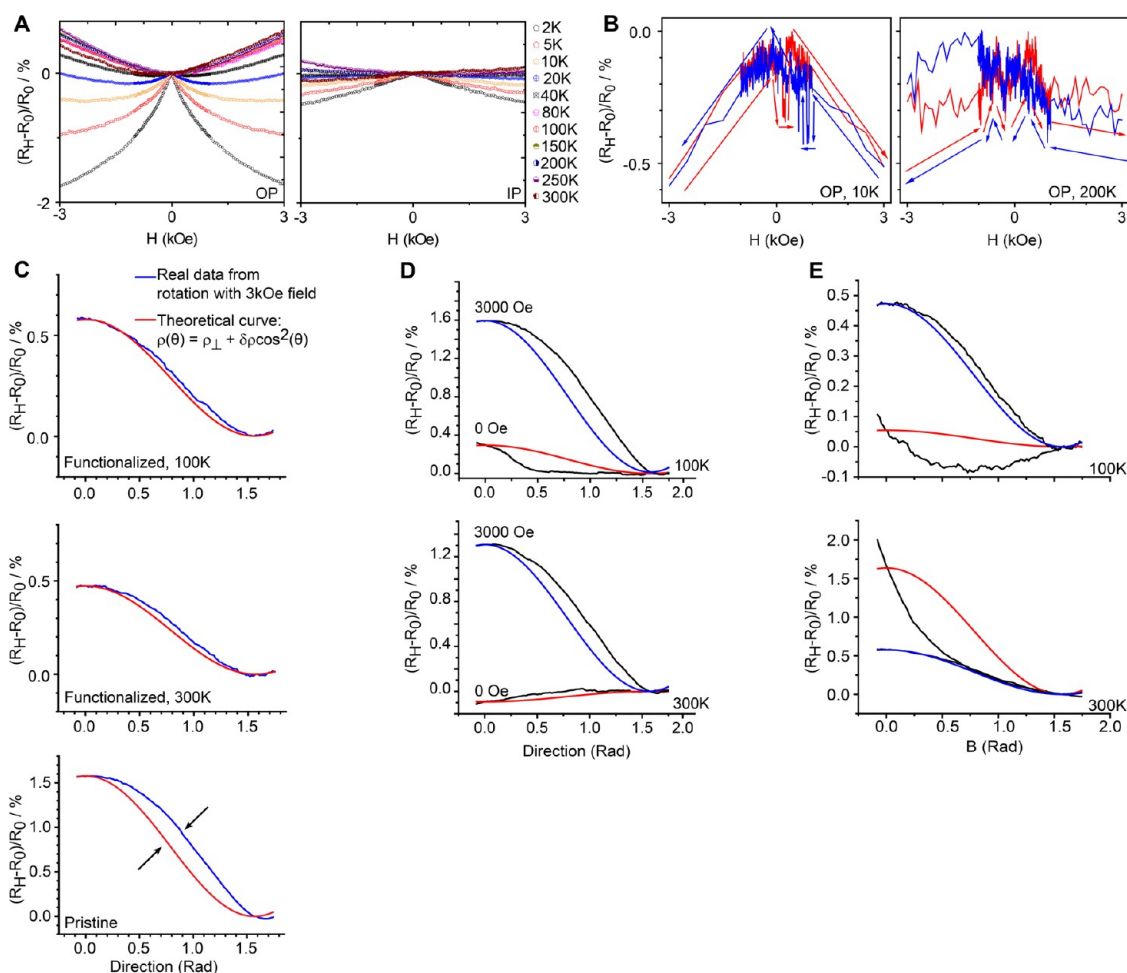
Figure 5. Magnetoresistance measurements: (A) out-of-plane and in-plane components in functionalized graphene. (B) GMR effects in the out-of-plane component at 10 and 200 K. (C) Anisotropic magnetoresistance (AMR) induced by the rotation of functionalized graphene at 100 and 300 K and pristine at 300 K. (D) AMR effects in pristine graphene at 100 and 300 K. (E) AMR effects in functionalized graphene at 100 and 300 K.

the two atoms in the graphene unit cell inequivalent with respect to the electronic transport, although no known chemical consequence occurs from this weak localization (WL) effect. In low magnetic fields, the effect of WL can be observed at low temperatures through a negative magnetoresistance with a peak at $B = 0$, as shown in Figure 5A. In higher magnetic fields, a positive magnetoresistance is observed; this magnetoresistance has been described as a weak antilocalization effect.[47,48] This positive magnetoresistance effect has been reproduced by many other research groups and is often reported as a linear MR (LMR) at room temperature. A quantum LMR effect is a signature of 2D magnetotransport behavior.[49,50]

After functionalization with a nitrophenyl group, a large negative magnetoresistance is observed at low temperatures and becomes positive above $T = 20$ K over the entire magnetic field (Figure 5A). In superparamagnetic films below the blocking temperature, most carrier transport pathways are forbidden because the adjacent domains freeze in the oppositely polarized magnetic states, causing an increase in the resistivity.

The application of a magnetic field then aligns the magnetic domains, and a negative magnetoresistance is observed. Recently, a large negative in-plane magnetoresistance was observed in graphene nanoribbons; this magnetoresistance was tentatively ascribed to edge effects on the electronic confinement.[51] Pristine epitaxial graphene exhibits a relatively small negative magnetoresistance, which increases marginally after functionalization with nitrophenyl (Figure 5A).[12,36]

The observed positive and negative MR effects were associated with weak antilocalization (WAL) and WL, respectively. The WAL effect, a signature of isospin-conserving transport, was suppressed by the WL effect in temperature ranges from 0 to approximately 150 K and from 0 to above room temperature in the pristine and functionalized samples, respectively. The suppression temperature echoed the temperature at which the slope of the temperature dependence on the zero-field resistance changed from negative to positive. This WAL effect was investigated in a tilted magnetic field at room temperature. The long-range scattering indicated a strong spin−orbit interaction.

A large negative magnetoresistance was observed with WL at reduced temperatures. This observation indicates a transition from the Anderson localization to a WL, and this transition is caused by giant magnetoresistance effects. Out-of-plane antiferromagnetic coupling could result in the GMR effect, although the GMR ratio is small compared to that of most efficient spin transport studies on epitaxial graphene.[52] However, the spin valve effect was observed, as shown in Figures 5B and S4C. The shifts in the negative magnetoresistance strongly indicate a typical antiferromagnetic coupling of the out-of-plane component at lower temperatures (observed up to room temperature). Because the contribution of the 2D segments is dominant in the perpendicular direction, the out-of-plane component behaves as an antiferromagnetic, ferromagnetic, or mixed state, although the antiferromagnetic state is dominant across the entire temperature range.

The anisotropic MR (AMR) reflects spin−orbit coupling. For the ferromagnetic exchange coupling, the conductance strongly depends on the magnetization direction and results in the AMR. For the functionalized sample, the AMR is perfectly fitted by a theoretical graph at 100 and 300 K, as shown in Figure 5C. For the pristine sample, the AMR is shifted left from the theoretical graph at 100 K, as shown in Figure 5D. The observed phenomenon is summarized in Figure 5E. This effect is found in ferromagnets, and the AMR effects of the 3D alloys are typically smaller than 5%.

The magnetotransport experiments indicate that a radical chemical functionalization might substantially increase the number of interacting unpaired local spins. Additionally, this negative magnetoresistance implies the prevention of ferromagnetic coupling between neighboring atoms; spins in relatively small 2D regions are aligned antiferromagnetically.

Brief Comparison with Other Organic Ferromagnets. There have been a number of reports on organic ferromagnets; however, their Curie ordering transitions typically occur far below room temperature.[53] In 1991, the first reproducible experimental observations of magnetism in p-block compounds were reported, in which magnetic ordering was observed in crystalline p-nitrophenyl nitronyl nitroxide (p-NPNN). The Curie temperature was 0.6 K for the molecular crystals of this ferromagnetic ordering. Each molecular radical unit bore a single, uncompensated electron spin.[54,55] The first charge transfer ferromagnet, $[Fe(C_5Me_5)_2][TCNE]$, had a Curie temperature of $T_c = 4.8$ K and a coercivity of $H_c = 1000$ Oe (at 2 K);[56] this ferromagnet was followed by $(TDAE)_{0.86}(C_{60})$, with $T_c = 16.1$ K and a saturation magnetization $M_{sat} = 0.1 \ \mu_B$/mol,[57] and $(BBTDA)(GaCl_4)$ with $T_c = 7$ K and $M_{sat} = 0.1 \ \mu_B$/mol.[58] Ferromagnetic neutral radicals have also been detected; for p-NC-C_6H_4-CN_2S_2 $T_c = 36$ K and $M_{sat} = 1.5 \times 10^{-3} \ \mu_B$/mol (at 0 K).[59] A series of ferromagnetic main-group radicals was discovered by Oakley and co-workers,[60−62] who characterized the compound $C_7H_5C_lN_3Se_4$ and found $T_c = 17$ K, $H_c = 1370$ Oe (at 2 K), and $M_{sat} = 1.03 \ \mu_B$/mol.

A study of the ferromagnetic defects at the grain boundaries in graphite yielded in-plane results of $T_c > 300$ K, $M_{sat} = 5.4 \times 10^{-6} \ \mu_B$/C, and $H_c = 7.7$ Oe (at 5 K).[20] Recently, partially hydrogenated EG exhibited $M_{sat} = 0.2 \ \mu_B$/C and $H_c \approx 40$ Oe at room temperature.[30] In contrast, NP-EG exhibited $M_{sat} = 0.1 \ \mu_B$/C (0.5 μ_B/NP functionality), with $H_c \approx 200$ Oe in-plane and 40 Oe out-of-plane. Graphite-based ferromagnets are characterized by high Curie temperatures because of the strong coupling present in the π-system. Based on a variety of m-H loop measurement techniques, the expected Curie temperature was found to be higher than that of nickel at approximately 500 K.

CONCLUSIONS

The main objective of this study was to reconfirm the presence of magnetic order in NP-functionalized graphene nanostructures through a new set of experimental data and attempt to correlate the new findings with our previously reported results. In particular, we presented five new findings to shed light on the origin of magnetism in graphene: (1) the field dynamics of microscale graphene acquired through AF-MFM measurements, (2) MOKE measurements indicating magnetic ordering along the primary graphene directions, (3) the presence of chemically isolated nanoribbons (CINs) observed by macroscale measurements (through VSM with a 30° rotation and microscale (through STM) measurements, (4) GMR effects supporting antiferromagnetic ordering, and (5) AMR effects reflecting the 2D nature of nanostructures in a mesoscopic system. The main results and implications are summarized as follows.

To the best of our knowledge, this is the first study to demonstrate MOKE effects in graphene nanostructures. In addition, focused transmission MOKE (Faraday effect) measurements confirmed the presence of antiferromagnetic ordering in the out-of-plane component, which is in agreement with our VSM and SQUID results. Field dynamics measured via AF-MFM (applied-field MFM) also confirmed antiferromagnetic coupling and indicated a nonzero remnant magnetization and, consequently, long-range magnetic order.[41] One of the most significant observations was the presence of chemically isolated nanoribbon structures (CINs) based on angle-dependent measurements through VSM and field-applied STM. The presence of CINs was also evidenced by angle-dependent measurements. We hypothesized that the symmetry could be broken by the functionalized sites in certain orientations (3,4 functionalities), which resulted in an amplification of the ferromagnetism along these specific orientations. Specifically, conjugation of the six-membered ring structure of graphene would be disrupted when

functional groups were introduced to the carbon structure due to electron transfer to sp^3-bond formation. The conversion of the sp^2 carbon hybridization to sp^3 rehybridization would break the symmetry, causing a breathing mode of the six-membered sp^2-carbon rings to be activated, which would give rise to a delocalized spin in the graphene π-system and would be expected to occur through spin alternation due to the presence of half-filled π-orbitals in the sp^2-bonded bipartite lattice of graphene. Note that, according to this hypothesis, the magnetism of functionalized graphene is not derived from a single layer of functionality or hydrogen atoms but instead from radical functionality with carbon atoms on the graphene structure.

We developed a systematic method for characterizing the field dynamics through field-dependent magnetic force microscopy. The AF-MFM measurements indicated that magnetization switching in the functionalized structures could be observed with a remnant magnetization of over 10 emu/cc.

The combination of aryl radical functionalization and epitaxially grown graphene is advantageous because it provides a large area and employs a gentle chemical process. Therefore, structural investigations ranging from the atomic level to the wafer level are feasible. We can also build systematic devices based on the position and coverage of the functionality. This nondisruptive process with the advantages of large area and gentle processing could be beneficial for engineering next-generation nanomagnetoelectronic/spintronic devices.

Our results demonstrated that large-area graphene with magnetic properties comparable to those of pristine graphene can be produced by epitaxial graphene processes. Hydrogenated graphene and other types of graphene exhibit similar magnetic properties. Aryl radical functionalized graphene can be used to build a 2D organic molecular magnet above room temperature. The exact values of the Curie and Neel temperatures were not determined, but the results implied that they could be near 500 K, which would be higher than that of nickel, a typical magnetic material.

This work also introduced well-developed comprehensive techniques for studying weak and nonuniform magnetic properties of transition states from paramagnetic to (anti)ferromagnetic behavior in 2D structures.

Finally, this study indicated the occurrence of spin transfer with a relatively long spin relaxation time. CINs can thus be used for extremely low energy spin switching. For example, one of the possible approaches would include spin transfer to CINs using well-developed nanoMTJ structures, as shown in Figure S7.[45]

It is important to note that the current comprehensive methodology could allow for magnetism control in the described functionalized 2D organic molecular magnets at high Curie temperatures. Both the spin-half paramagnetism and superparamagnetism were greater than those of the surface- and volume-averaged magnetometry with nonuniform or weak magnetic responses in graphene systems.[12,26] In addition, the epitaxial graphene systems functionalized with aryl radicals demonstrated two advantages for the controllability of magnetic properties: (1) chemical functionalization can provide more predictable results than systems with physical defects because the functionality attaches to the carbon atoms in a gentle manner, and (2) reduced graphene oxides and exfoliated graphene systems cannot create smooth surfaces at the macroscale. Graphene structures with large areas, such as CVD and graphene epitaxially grown on SiC, could allow for systematic measurements of changes in the planes. Moreover, the chemistry plays a significant role in demonstrating the systematic characteristics of the density and location of functionalities on the basal plane of the graphene. Optimization of the chemical functionalization of the EG wafers could yield long-range anti/ferromagnetic ordering and could form the basis for advanced spintronic devices.[9,63−68] The approach taken in the present work does not generate physical defects in the graphene lattice[26] but leads to systematic carbon−carbon bonds, which results in unpaired spins for engineering 2D magnetic devices such as energy-efficient current-induced magnetization switching with the advantage of long spin relaxation time in an organic macromolecule. This gentle "chemistry" approach (functionalized graphene) differs from physical approaches, which usually involve force factors (defective graphene), and could open a route to overcome the fundamental limitations of silicon-based microelectronics with the use of spintronics in a controllable way.

MATERIALS AND METHODS

Scanning Probe Microscopy Measurements. The SPM study was performed in noncontact mode using a Bruker-Nano AFM system (Santa Barbara, CA, U.S.A.). The EFM and MFM measurements were conducted in a dynamic lift mode with a lift distance of 30 nm. The dynamics were measured in the presence of a magnetic field by sweeping the field range between −60 and +60 Oe.

Magneto-Optical Kerr Microscopy (MOKE). The Kerr measurements were performed with a focused MOKE system in transmission mode. The light source was directed toward the sample, which

was located between the poles of an electromagnet that could reach 3.3 T (GMW Associate, San Carlos, CA, U.S.A.). A standard two-mirror setup allowed for adjustment of both the position of the light source and the angle of incidence.

Vibrating Sample Magnetometry (VSM). The m-H loop measurements were performed with the VSM option of a Quantum Design cryogenic physical property measurement system (PPMS) with a 9-T superconducting magnet. The samples were mounted on a quartz paddle with regular disk holders, and GE-7031 varnish was used to withstand the thermal cycling. To optimize the approach, the samples were mounted with a

35-mm upward offset. To check the background signal, each sample measurement was preceded by measurements of empty sample holders and silicon carbide substrates. After subtraction, the SiC wafers generated a negligible magnetic signal. The magnetic field was swept at a rate of 10.139 Oe/sec.

Superconducting Quantum Interference Device (SQUID). To measure the DC magnetization in an MPMS system with a reciprocating sample option (RSO) adapter, the EG-SiC samples were loaded into plastic straws. In all measurements, the length of the graphite RSO transport rod was reduced by replacing the last segment with a straw. We found that the presence of the graphite rod close to the sample affected the measured signal.

Cryogenic Magnetotransport Measurements. To perform four-point resistance measurements, four in-line gold contacts (30 nm Pd, 100 nm Au) were deposited with an electron beam evaporator (Temescal BJD 1800 System) on the C-face of an EG substrate at room temperature. Then, the samples were wired with silver conductive adhesive paste (from Alfa Aesar). Indium wire (1 mm diameter and 99.999% purity) was used to connect the EG and bridge contacts. Cigarette paper was used to electrically isolate the sample from the user-printed circuit board.

Functionalization of the Epitaxial Graphene. The epitaxial graphene (EG) substrate was immersed in a solution of 10 mM 4-nitrophenyl diazonium (NPD) tetrafluoroborate and 0.1 M tetrabutylammonium hexafluoro-phosphate ([Bu$_4$N]PF$_6$]) in degassed acetonitrile (ACN) for 20 h in a glovebox in the dark. Then, the substrate was removed and washed with ACN and acetone.[34]

Conflict of Interest: The authors declare no competing financial interest.

Supporting Information Available: Additional data sets and figures are included. This material is available free of charge *via* the Internet at http://pubs.acs.org.

REFERENCES AND NOTES

1. Berger, C.; Song, Z.; Li, T.; Li, X.; Ogbazghi, A. Y.; Feng, R.; Dai, Z.; Marchenkov, A. N.; Conrad, E. H.; First, P. N.; *et al.* Ultrathin Epitaxial Graphite: 2D Electron Gas Properties and a Route toward Graphene-based Nanoelectronics. *J. Phys. Chem. B* **2004**, *108*, 19912–19916.

2. Novoselov, K. S.; Geim, A. K.; Morozov, S. V.; Jiang, D.; Katsnelson, M. I.; Grigorieva, I. V.; Dubonos, S. V.; Firsov, A. A. Two-Dimensional Gas of Massless Dirac Fermions in Graphene. *Nature* **2005**, *438*, 197–200.

3. Stankovich, S.; Dikin, A.; Dommett, G. H. B.; Kohlhaas, K. M.; Zimney, E. J.; Stach, E. A.; Piner, R. D.; Nguyen, S. T.; Ruoff, R. S. Graphene-Based Composite Materials. *Nature* **2006**, *442*, 282–286.

4. Bolotin, K. I.; Sikes, K. J.; Hone, J.; Stormer, H. L.; Kim, P. Temperature-Dependent Transport in Suspended Graphene. *Phys. Rev. Lett.* **2008**, *101*, 096802.

5. Lee, C.; Wei, X.; Kysar, J. W.; Hone, J. Measurement of the Elastic Properties and Intrinsic Strength of Monolayer Graphene. *Science* **2008**, *321*, 385–388.

6. Nair, R. R.; Blake, P.; Grigorenko, A. N.; Novoselov, K. S.; Booth, T. J.; Stauber, T.; Peres, N. M. R.; Geim, A. K. Fine Structure Constant Defines Visual Transparency of Graphene. *Science* **2008**, *320*, 1308.

7. Cai, J.; Ruffieux, P.; Jaafar, R.; Bieri, M.; Braun, T.; Blankenburg, S.; Muoth, M.; Seitsonen, A. P.; Saleh, M.; Feng, X.; *et al.* Atomically Precise Bottom-up Fabrication of Graphene Nanoribbons. *Nature* **2010**, *466*, 470–473.

8. Esquinazi, P.; Spemann, D.; Höhne, R.; Setzer, A.; Han, K. H.; Butz, T. Induced Magnetic Ordering by Proton Irradiation in Graphite. *Phys. Rev. Lett.* **2003**, *91*, 227201.

9. Wolf, S. A.; Awschalom, D. D.; Buhrman, R. A.; Daughton, J. M.; von Molnar, S.; Roukes, M. L.; Chtchelkanova, A. Y.; Treger, D. M. Spintronics: A Spin-Based Electronics Vision for the Future. *Science* **2001**, *294*, 1488–1495.

10. Yazyev, O. V. Magnetism in Disordered Graphene and Irradiated Graphite. *Phys. Rev. Lett.* **2008**, *101*, 037203.

11. Son, Y. W.; Cohen, M. L.; Louie, S. G. Half-Metallic Graphene Nanoribbons. *Nature* **2006**, *444*, 347.

12. Hong, J.; Niyogi, S.; Bekyarova, E.; Itkis, M. E.; Palanisamy, R.; Litvinov, D.; Berger, C.; de Heer, W. A.; Khizroev, S.; Haddon, R. C. Effect of Nitrophenyl Functionalization on the Magnetic Properties of Epitaxial Graphene. *Small* **2011**, *7*, 1175–1180.

13. Smith, C. I.; Miyaoka, H.; Ichikawa, T.; Jones, M. O.; Harmer, J.; Ishida, W.; Edwards, P. P.; Kojima, Y.; Fuji, H. Electron Spin Resonance Investigation of Hydrogen Absorption in Ball-Milled Graphite. *J. Phys. Chem. C* **2009**, *113*, 5409–5416.

14. Esquinazi, P.; Setzer, A.; Höhne, R.; Semmelhack, C.; Kopelevich, Y.; Spemann, D.; Butz, T.; Kohlstrunk, B.; Lösche, M. Ferromagnetism in Oriented Graphite Samples. *Phys. Rev. B* **2002**, *66*, 024429.

15. Kopelevich, Y.; Esquinazi, P.; Torres, J. H. S.; Moehlecke, S. Ferromagnetic- and Superconducting-Like Behavior of Graphite. *J. Low Temp. Phys.* **2000**, *119*, 691–702.

16. da Silva, R.; Torres, H.; Kopelevich, Y. Indication of Superconductivity at 35 K in Graphite-Sulfur Composites. *Phys. Rev. Lett.* **2001**, *87*, 147001.

17. Mombrú, A. W.; Pardo, H.; Faccio, R.; de Lima, O. F.; Leite, E. R.; Zanelatto, G.; Lanfredi, A. J. C.; Cardoso, C. A.; Araújo-Moreira, F. M. Multilevel Ferromagnetic Behavior of Room-Temperature Bulk Magnetic Graphite. *Phys. Rev. B* **2005**, *71*, 100404(R).

18. Esquinazi, P.; Höhne, R. Magnetism in Carbon Structures. *J. Magn. Magn. Mater.* **2005**, *290–291*, 20–27.

19. Esquinazi, P.; Barzola-Quiquia, J.; Spemann, D.; Rothermel, M.; Ohldag, H.; Garcia, N.; Setzer, A.; Butz, T. Magnetic Order in Graphite: Experimental Evidence, Intrinsic and Extrinsic Difficulties. *J. Magn. Magn. Mater.* **2010**, *332*, 1156–1161.

20. Cervenka, J.; Katsnelson, M. I.; Flipse, C. F. J. Room-Temperature Ferromagnetism in Graphite Driven by Two-Dimensional Networks of Point Defects. *Nat. Phys.* **2009**, *5*, 840–844.

21. Martínez-Martín, D.; Jaafar, M.; Pérez, R.; Gómez-Herrero, J.; Asenjo, A. Upper Bound for the Magnetic Force Gradient in Graphite. *Phys. Rev. Lett.* **2010**, *105*, 257203.

22. Ebert, L. B. Intercalation Compounds of Graphite. *Annu. Rev. Mater. Sci.* **1976**, *6*, 181–211.

23. DiSalvo, F. J.; Safran, S. A.; Haddon, R. C.; Waszczak, J. V.; Fischer, J. E. Large Anisotropy and Stage Dependence of the Magnetic Susceptibility of Alkali-Graphite Intercalation Compounds. *Phys. Rev. B* **1979**, *20*, 4883–4888.

24. Ćirić, L.; Sienkiewicz, A.; Náfrádi, B.; Mionić, M.; Magrez, A.; Forró, L. Towards Electron Spin Resonance of Mechanically Exfoliated Graphene. *Phys. Status Solidi B* **2009**, *246*, 2558–2561.

25. Sepioni, M.; Nair, R. R.; Rablen, S.; Narayanan, J.; Tuna, F.; Winpenny, R.; Geim, A. K.; Grigorieva, I. V. Limits on Intrinsic Magnetism in Graphene. *Phys. Rev. Lett.* **2010**, *105*, 207205.

26. Nair, R. R.; Sepioni, M.; Tsai, I. L.; Lehtinen, O.; Keinonen, J.; Krasheninnikov, A. V.; Thomson, T.; Geim, A. K.; Grigorieva, I. V. Spin-Half Paramagnetism in Graphene Induced by Point Defects. *Nat. Phys.* **2012**, *8*, 199–202.

27. Wang, Y.; Huang, Y.; Song, Y.; Zhang, X.; Ma, Y.; Liang, J.; Chen, Y. Room-Temperature Ferromagnetism of Graphene. *Nano Lett.* **2009**, *9*, 220–224.

28. Ramakrishna Matte, H. S. S.; Subrahmanyam, K. S.; Rao, C. N. R. Novel Magnetic Properties of Graphene: Presence of Both Ferromagnetic and Antiferromagnetic Features and Other Aspects. *J. Phys. Chem. C* **2009**, *113*, 9982–9985.

29. Tada, K.; Haruyama, J.; Yang, H. X.; Chshiev, M.; Matsui, T.; Fukuyama, H. Graphene Magnet Realized by Hydrogenated Graphene Nanopore Arrays. *Appl. Phys. Lett.* **2011**, *99*, 183111.

30. Xie, L.; Wang, X.; Lu, J.; Ni, Z.; Luo, Z.; Mao, H.; Wang, R.; Wang, Y.; Huang, H.; Qi, D.; *et al.* Room Temperature

Ferromagnetism in Partially Hydrogenated Epitaxial Graphene. *Appl. Phys. Lett.* **2011**, *98*, 193113.

31. Giesbers, A. J. M.; Uhlířová, K.; Konečný, M.; Peters, E. C.; Burghard, M.; Aarts, J.; Flipse, C. F. J. Interface Induced Room-Temperature Ferromagnetism in Hydrogenated Epitaxial Graphene. *arXiv.org, e-Print Arch.* **2013**, *1305*, 3158.

32. Garnica, M.; Stradi, D.; Barja, S.; Calleja, F.; Díaz, C.; Alcamí, M.; Martín, N.; Vázquez de Parga, A. L.; Martín, F.; Miranda, R. Long-Range Magnetic Order in a Purely Organic 2D Layer Adsorbed on Epitaxial Graphene. *Nat. Phys.* **2013**, *9*, 368–374.

33. Nair, R. R.; Tsai, I. L.; Sepioni, M.; Lehtinen, O.; Keinonen, J.; Krasheninnikov, A. V.; Castro Neto, A. H.; Katsnelson, M. I.; Geim, A. K.; Grigorieva, I. V. Dual Origin of Defect Magnetism in Graphene and Its Reversible Switching by Molecular Doping. *Nat. Commun.* **2013**, *4*, 2010.

34. Bekyarova, E.; Itkis, M. E.; Ramesh, P.; Berger, C.; Sprinkle, M.; de Heer, W. A.; Haddon, R. C. Chemical Modification of Epitaxial Graphene: Spontaneous Grafting of Aryl Groups. *J. Am. Chem. Soc.* **2009**, *131*, 1336–1337.

35. Niyogi, S.; Bekyarova, E.; Itkis, M. E.; Zhang, H.; Shepperd, K.; Hick, J.; Sprinkle, M.; Berger, C.; Lau, C.; de Heer, W. A. Spectroscopy of Covalently Functionalized Graphene. *Nano Lett.* **2010**, *10*, 4061–4066.

36. Niyogi, S.; Bekyarova, E.; Hong, J.; Khizroev, S.; Berger, C.; de Heer, W. A.; Haddon, R. C. Covalent Chemistry for Graphene Electronics. *J. Phys. Chem. Lett.* **2011**, *2*, 2487–2498.

37. Ryu, S.; Han, M. Y.; Maultzsch, J.; Heinz, T. F.; Kim, P.; Steigerwald, M.; Brus, L. E. Reversible Basal Plane Hydrogenation of Graphene. *Nano Lett.* **2008**, *8*, 4597–4602.

38. Liu, H.; Ryu, S.; Chen, Z.; Steigerwald, M. L.; Nuckolls, C.; Brus, L. E. Photochemical Reactivity of Graphene. *J. Am. Chem. Soc.* **2009**, *131*, 17099–17101.

39. Robinson, J. A.; Wetherington, M.; Tedesco, J. L.; Campbell, P. M.; Weng, X.; Stitt, J.; Fanton, M. A.; Frantz, E.; Snyder, D.; Van Mil, B. Correlating Raman Spectral Signatures with Carrier Mobility in Epitaxial Graphene: A Guide to Achieving High Mobility on the Wafer Scale. *Nano Lett.* **2009**, *9*, 2873–2876.

40. de Heer, W. A.; Berger, C.; Wu, X.; First, P. N.; Conrad, E. H.; Li, X.; Li, T.; Sprinkle, M.; Hass, J.; Sadowski, M. L.; *et al.* Epitaxial Graphene. *Solid State Commun.* **2007**, *143*, 92–100.

41. Hong, J.; Bekyarova, E.; Likang, P.; de Heer, W. A.; Haddon, R. C.; Khizroev, S. Room-Temperature Magnetic Ordering in Functionalized Graphene. *Sci. Rep.* **2012**, *2*, 624.

42. Hong, J.; Niyogi, S.; Bekyarova, E.; Itkis, M. E.; Ramesh, P.; Berger, C.; de Heer, W. A.; Haddon, R. C.; Khizroev, S. Effect of Functionalization on the Electrostatic Charging, Tunneling, and Raman Spectroscopy of Epitaxial Graphene. *J. Vac. Sci. Technol., B* **2012**, *30*, 03D103.

43. Crassee, I.; Levallois, J.; Walter, A. L.; Ostler, M.; Bostwick, A.; Rotenberg, E.; Seyller, T.; van der Marel, D.; Kuzmenko, A. B. Giant Faraday Rotation in Single- and Multilayer Graphene. *Nat. Phys.* **2011**, *7*, 48–51.

44. Cheng, J. L.; Salazar, C.; Sipe, J. E. Optical Properties of Functionalized Graphene. *Phys. Rev. B* **2013**, *88*, 045438.

45. Hong, J.; Liang, P.; Safonov, V.; Khizroev, S. Energy-Efficient Spin-Transfer Torque Magnetization Reversal in Sub-10-nm Magnetic Tunneling Junction Point Contacts. *J. Nanopart. Res.* **2013**, *15*, 1–6.

46. Thomas, L.; Lionti, F.; Ballou, R.; Gatteschi, D.; Sessoli, R.; Barbara, B. Macroscopic Quantum Tunneling of Magnetization in a Single Crystal of Nanomagnets. *Nature* **1996**, *383*, 145–147.

47. Morozov, S. V.; Novoselov, K. S.; Katsnelson, M. I.; Schedin, F.; Ponomarenko, L. A.; Jiang, D.; Geim, A. Strong Suppression of Weak Localization in Graphene. *Phys. Rev. Lett.* **2006**, *97*, 016801.

48. Wu, X.; Li, X.; Song, Z.; Berger, C.; de Heer, W. A. Weak Antilocalization in Epitaxial Graphene: Evidence for Chiral Electrons. *Phys. Rev. Lett.* **2007**, *98*, 136801.

49. Friedman, A. L.; Tedesco, J. L.; Campbell, P. M.; Culbertson, J. C.; Aifer, E.; Perkins, F. K.; Myers-Ward, R. L.; Hite, J. K.; Eddy, C. R., Jr.; Jernigan, G. G.; *et al.* Quantum Linear Magnetoresistance in Multilayer Epitaxial Graphene. *Nano Lett.* **2010**, *10*, 3962.

50. Singh, R. S.; Wang, X.; Chen, W.; Ariando; Wee, A. T. S. Large Room-temperature Quantum Linear Magnetoresistance in Multilayered Epitaxial Graphene: Evidence for Two-dimensional Magnetotransport. *Appl. Phys. Lett.* **2013**, *103*, 049902.

51. Bai, J.; Cheng, R.; Xiu, F.; Liao, L.; Wang, M.; Shailos, A.; Wang, K. L.; Huang, Y.; Duan, X. Very Large Magnetoresistance in Graphene Nanoribbons. *Nat. Nanotechnol.* **2010**, *5*, 655–659.

52. Dlubak, B.; Martin, M. B.; Deranlot, C.; Servet, B.; Xavier, S.; Mattana, R.; Sprinkle, M.; Berger, C.; de Heer, W. A.; Petroff, F.; *et al.* Highly Efficient Spin Transport in Epitaxial Graphene on SiC. *Nat. Phys.* **2012**, *8*, 557–561.

53. Miller, J. S.; Epstein, A. J. *Encyclopedia of Smart Materials*; Harvey, J., Ed.; Wiley & Sons: New York, 2002; p 591.

54. Takahashi, M.; Turek, P.; Nakazawa, Y.; Tamura, M.; Nozawa, K.; Shiomi, D.; Ishikawa, M.; Kinoshita, M. Discovery of a Quasi-1D Organic Ferromagnet, p-NPNN. *Phys. Rev. Lett.* **1991**, *67*, 746–748.

55. Tamura, M.; Hosokoshi, Y.; Shiomi, D.; Kinoshita, M.; Nakazawa, Y.; Ishikawa, M.; Sawa, H.; Kitazawa, T.; Eguchi, A.; Nishio, A.; *et al.* Magnetic Properties and Structures of the α- and δ-Phases of p-NPNN. *Phys. Soc. Jpn.* **2003**, *72*, 1735–1744.

56. Miller, J. S.; Calabrese, J. C.; Epstein, A. J.; Bigelow, R. W.; Zhang, J. H.; Reiff, W. M. Ferromagnetic Properties of One-Dimensional Decamethylferrocenium Tetracyanoethylenide (1:1):[Fe(η_5-C$_5$Me$_5$)$_2$]$^{\bullet+}$[TCNE]$^{\bullet-}$. *J. Chem. Soc., Chem. Commun.* **1986**, *2986*, 1026–1028.

57. Allemand, P. M.; Khemani, K. C.; Koch, A.; Wudl, F.; Holczer, K.; Donovan, S.; Gruner, G.; Thompson, J. D. Organic Molecular Soft Ferromagnetism in a Fullerene C60. *Science* **1991**, *253*, 301–303.

58. Fujita, W.; Awaga, K. Crystal Structure and Magnetic Properties of a Thiazyl Organic Ferromagnet, BBDTA·GaCl$_4$ with T_C = 7.0 K. *Chem. Phys. Lett.* **2004**, *388*, 186–189.

59. Banister, A. J.; Bricklebank, N.; Lavender, I.; Rawson, J. M.; Gregory, C. I.; Tanner, B. K.; Clegg, W.; Elsegood, M. R.; Palacio, F. Spontaneous Magnetization in a Sulfur−Nitrogen Radical at 36 K. *Angew. Chem., Int. Ed.* **1996**, *35*, 2533–2535.

60. Robertson, C. M.; Leitch, A. A.; Cvrkalj, K.; Reed, R. W.; Myles, D. J. T.; Dube, P. A.; Oakley, R. T. J. Enhanced Conductivity and Magnetic Ordering in Isostructural Heavy Atom Radicals. *J. Am. Chem. Soc.* **2008**, *130*, 8414–8425.

61. Robertson, C. M.; Leitch, A. A.; Cvrkalj, K.; Myles, D. J. T.; Reed, R. W.; Dube, P. A.; Oakley, R. T. Ferromagnetic Ordering in Bisthiaselenazolyl Radicals: Variations on a Tetragonal Theme. *J. Am. Chem. Soc.* **2008**, *130*, 14791–14801.

62. Leitch, A. A.; Yu, X.; Winter, S. M.; Secco, R. A.; Dube, P. A.; Oakley, R. T. Structure and Property Correlations in Heavy Atom Radical Conductors. *J. Am. Chem. Soc.* **2009**, *131*, 7112–7125.

63. Tombros, N.; Jozsa, C.; Popinciuc, M.; Jonkman, H. T.; van Wees, B. J. Electronic Spin Transport and Spin Precession in Single Graphene Layers at Room Temperature. *Nature* **2007**, *448*, 571–575.

64. Yazyev, O. V. Emergence of Magnetism in Graphene Materials and Nanostructures. *Rep. Prog. Phys.* **2010**, *73*, 056501.

65. Pisani, L.; Montanari, B.; Harrison, N. M. A Defective Graphene Phase Predicted to be a Room Temperature Ferromagnetic Semiconductor. *New J. Phys.* **2008**, *10*, 033002.

66. Santos, E. J. G.; Ayuela, A.; Sanchez-Portal, D. Universal Magnetic Properties of sp^3-type Defects in Covalently Functionalized Graphene. *New J. Phys.* **2012**, *14*, 043022.

67. Santos, E. J. G. Magnetoelectric Effect in Functionalized Few-layer Graphene. *Phys. Rev. B* **2013**, *87*, 155440.

68. Santos, E. J. G. Electrical Spin Switch in Hydrogenated Multilayer Graphene. *J. Chem. Phys. C* **2013**, *117*, 6420.